RSC Advances

PAPER

View Article Online
View Journal | View Issue

Cite this: *RSC Adv.*, 2022, **12**, 31546

Synthesis and optical properties of $Gd_4Al_2O_9:Eu^{3+}$, a red emitting phosphor with a strong negative thermal quenching effect

Junyu Ming,[a] Chaolian Luo,[a] Shaokun Ling,[a] Chang Chen,[a] Yaxiong Wang,[a] Sen Liao,*[ab] Yingheng Huang*[ab] and Jie Liang*[b]

Received 3rd September 2022
Accepted 18th October 2022

DOI: 10.1039/d2ra05540f

rsc.li/rsc-advances

For the purpose of obtaining red-light phosphors with excellent luminescence thermal stability, a series of $Gd_4Al_2O_9:Eu^{3+}$ (GAO:Eu^{3+}) phosphors were synthesized by combining the sol-gel method with high-temperature calcination, and a detailed series of study and analysis of their room temperature and high temperature luminescence properties was carried out. In GAO, the emission peaks corresponding to the $^5D_0 \rightarrow {}^7F_j$ (j = 0, 1, 2, 3 and 4) transitions of Eu^{3+} were observed at 578, 590, 610, 654, and 707 nm, with the strongest emission peak at 610 nm, and the obtained samples were red-light phosphors. The sample GAO:Eu^{3+} synthesized by combining the sol-gel method with high-temperature calcination has a negative thermal quenching (NTQ) effect, and the best doped sample GAO:0.16Eu^{3+} has an optimal luminescence temperature of 120 °C, and the corresponding integrated PL intensity is 183.2% of the initial value at 30 °C. The presence of the NTQ effect makes GAO:0.16Eu^{3+} have good luminescence thermal stability, which manifests as thermal-optical energy conversion at the macroscopic level. A detailed study of the thermal quenching mechanism was carried out.

1. Introduction

White light emitting diodes (WLEDs) are considered to be the most promising green solid-state lighting devices for the twenty-first century, with applications in lighting, exhibitions, electronic devices and other fields. Compared to previous incandescent and fluorescent lamps, WLEDs have excellent properties such as high luminous efficiency, energy efficiency, long lifetime and environmental friendliness.[1] Some phosphor-converted white light emitting LEDs (Pc-WLEDs) currently on the market are a combination of three phosphors that can produce red, green and blue light (RGB) respectively, but the WLEDs prepared by this method are sensitive to the device operating temperature, and the color rendering index (CRI) and correlated color temperature (CCT) are prone to change. The performance of red emitting phosphors is relatively poor compared to the luminescent performance of green and blue emitting phosphors available in the market. Conventional sulphide red emitting phosphors such as (Ca,Sr)S:Eu^{2+} and $Y_2O_2S:Eu^{3+}$ are unstable at high temperatures and under humid conditions. The synthesis of Eu^{2+} doped (oxygenated) nitrides require harsh preparation conditions and often suffers from blue–green light reabsorption, resulting in imbalance in color and reduced luminous efficiency.[2,3] A good quality red emitting phosphor for lamps should be able to be excited by near-UV light (370–410 nm) without reabsorption of visible light and have good chemical stability. In addition, the operating temperature of Pc-WLEDs is over 150 °C, so the ability to maintain excellent fluorescence emission at operating temperature is an important indicator to evaluate the phosphor performance. For most phosphors, the emission intensity decreases with increasing temperature, *i.e.*, a thermal quenching phenomenon, which severely degrades the white light quality of WLEDs.[4] Therefore, the synthesis of red emitting phosphors with high luminescence thermal stability is very important to obtain high quality warm white light.

Eu^{3+} is recognized as an excellent choice for emitting phosphor luminescence centers,[5,6] and in various matrixes under near-UV excitation can emit high-quality red light produced by the $^5D_0 \rightarrow {}^7F_j$ (j = 0, 1, 2, 3 and 4) transition, such as Mg_2LaTaO_6,[7] $Na_2Ca_2Nb_4O_{13}$,[8] $KGdF_4$,[9] $NaLaTi_2O_6$,[10] *etc.* For Eu^{3+}, the choice of substrate is very important. In recent years, a lot of research has been carried out on Ln_2O_3–Al_2O_3 (Ln = rare earth ion) compounds, which are widely used in solid-state laser materials, scintillators for medical imaging, WLEDs lighting, displays, *etc.*, because of their high chemical and thermal stability, high creep resistance, and ability to incorporate different lanthanide ions for better luminescence.[11–14] GAO, a member of the Ln_2O_3–Al_2O_3 family

[a]School of Resources, Environment and Materials, Guangxi University, Nanning, Guangxi, 530004, China. E-mail: liaosen@gxu.edu.cn; huangyingheng@163.com
[b]School of Chemistry and Chemical Engineering, Guangxi University, Nanning, Guangxi, 530004, China. E-mail: liangj@gxu.edu.cn; Fax: +86 771 3233718; Tel: +86 771 3233718

of compounds, also has these characteristics and is an excellent choice as a matrix for Eu^{3+}-doped phosphors. For example, Li *et al.*[15] reported the synthesis of GAO:Eu^{3+} phosphors by applying a co-precipitation method, Singh *et al.*[14] applied a urea-assisted combustion method to synthesize GAO:Eu^{3+} phosphors, and Deng *et al.*[16] synthesized GAO:Er^{3+}/Yb^{3+} upconversion phosphors by co-precipitation method. However, in our limited literature research, we have not found any report on the synthesis of near-UV-excited GAO:Eu^{3+} red phosphors by combining a sol-gel method with two-stage high-temperature calcination.

The operating temperature of high-power WLEDs is around 200 °C, therefore, if the phosphor in the WLEDs operating temperature range exists thermal quenching will seriously affect the light quality of WLEDs, while the current commercial phosphors in this problem has not been well solved, for example, commercial phosphors YAG:Ce^{3+}, (Sr,Ca)$AlSiN_3$:Eu^{2+} and $SrSi_2O_2N_2$:Eu^{2+} at 200 °C corresponding to the percentage loss of emitted light intensity of 12%, 18% and 20%, respectively. In order to overcome thermal quenching, researchers have tried to develop a variety of zero-thermal-quenching phosphors, of which more typically such as: Kang *et al.*[17] reported that $LuVO_4$:Bi^{3+} phosphor with an optimal luminescence temperature at 100 °C, Zhong *et al.*[18] reported that $La_3Si_6N_{11}$:Ce^{3+} zero-thermal-quenching phosphor with an optimal luminescence temperature at 75 °C, Chen *et al.*[19] reported that $Ba_3Y(PO_4)_3$:Ce^{3+}/Tb^{3+}/Mn^{2+}phosphor at an optimal luminescence temperature of 152 °C, Qiao *et al.*[20] reported that $K_2BaCa(PO_4)_2$:Eu^{2+} phosphor at 200 °C still has 96% of the integrated luminescence intensity at an initial temperature of 25 °C, Fang *et al.*[21] reported that $LaAlO_3$:Ca^{2+}, Bi^{3+}, Mn^{4+} red light phosphor at 150 °C shows an integrated luminescence intensity 103% of the initial integrated intensity at 25 °C, *etc.* However, only a few reported Eu^{3+}-activated red phosphors showed zero-thermal-quenching, such as Zhao *et al.*[22] reported that $K_5Y(P_2O_7)$:Eu^{3+} at the optimal luminescence temperature of 100 °C with a luminescence integral intensity about 100.7% of that at the initial temperature of 25 °C, Wang *et al.*[23] reported that $LaSc_3(BO_3)_4$:Eu^{3+} red phosphor at the optimum luminescence temperature of 225 °C is about 132.5% of the integrated luminescence intensity at the initial temperature of 25 °C. Therefore, more research is needed to obtain Eu^{3+}-activated red phosphors with excellent high-temperature fluorescence stability. After a series of explorations, we obtained a GAO:Eu^{3+} red phosphor with excellent high-temperature fluorescence stability, the integrated luminescence intensity in the operating temperature range of 150–210 °C in high-power WLEDs always higher than 148.7% of the integrated luminescence intensity at the initial temperature of 30 °C, which was further improved than the previous ones in terms of fluorescence thermal stability.

In this paper, we prepared a series of GAO:Eu^{3+} phosphors by combining the sol-gel method with high-temperature calcination. The experimental results show that the synthesized GAO:Eu^{3+} phosphors have a strong NTQ effect and are near-UV excited red phosphors with excellent high-temperature fluorescence properties.

2. Experimental section

2.1. Reagent and apparatus

All chemicals were reagent-grade pure and purchased from the Sinopharm Chemical Reagent Co. Ltd, China.

Powder X-ray diffraction (XRD) was performed at a scanning rate of 5° min^{-1} from 5 to 70° for 2θ at room temperature by using a Rigaku D/max 2500 V diffractometer. It was equipped with a graphite monochromator by utilizing monochromatic CuKα radiation (λ = 0.154178 nm). Excitation and emission (PLE&PL) spectra were recorded at room temperature by a Horiba Fluoro Max-4-R F6000 equipped with a xenon lamp as the excitation source, the morphology was observed by SEM, and the elements were analyzed by EDS (EDS, Oxford INCA300, England).

2.2. Preparation of the samples

A series of GAO:Eu^{3+} phosphors were prepared by combining the sol-gel method with high-temperature calcination. Take the synthesis of 0.005 mol GAO:0.16Eu^{3+} as an example: (i) all kind of metal nitrates required for synthesis of 0.005 mol GAO:0.16Eu^{3+} ware weighted according to stoichiometric ratio, dissolved in 30 ml deionized water, and moved into a magnetic stirrer, and stirred evenly during water both heating; (ii) weight 0.06 mol citric acid and dissolve it in 20 ml deionized water; (iii) the citric acid solution obtained in step (ii) was added to the nitrate mixture in step (i) using a rubber-tipped burette in a uniform drop, after completion of the dropwise addition, a clear and viscous gel is obtained by adjusting the water bath temperature of the magnetic stirrer to 80 °C and stirring continuously for 4 h; (iv) the gel was dried in an oven at 120 °C for 15 h; (v) the fluffy dry gel from (iv) was removed and ground in a mortar to obtain a pale yellow powder; (vi) the yellowish powder was pre-fired at 900 °C for 4 h. After annealing, the powder was removed and ground, and then calcined in a muffle furnace at 1400 °C for 5 h. After annealing, the powder was removed and ground to obtain a white powder, *i.e.*, the target product.

3. Results and discussion

3.1 Structure, morphology and composition

As shown in Fig. 1(a), the XRD spectra of GAO:xEu^{3+} (x = 0.14–0.19) are compared with the standard card of GAO (PDF#46 – 0396). It can be seen from the Fig. 1(a) that the diffraction peaks of the sample basically correspond to the standard card, which proves that the pure phase GAO crystals without other heterogeneous phases generated. The indexed results of GAO:0.16Eu^{3+} are shown in Table 1. Because of lanthanide shrinkage, the radius of Gd^{3+} is smaller than that of Eu^{3+}. Since some of Gd^{3+} ions have been replaced by Eu^{3+} ions in GAO:0.16Eu^{3+}, Table 1 shows that the unit cell volume of sample GAO:0.16Eu^{3+} is slightly larger than that of PDF#46 – 0396.

According to Vegard's law,[8] the radius of metal ions does not exceed 15% and they can easily replace each other. The difference in ionic radius between Gd^{3+} and Eu^{3+} is within 15%, and

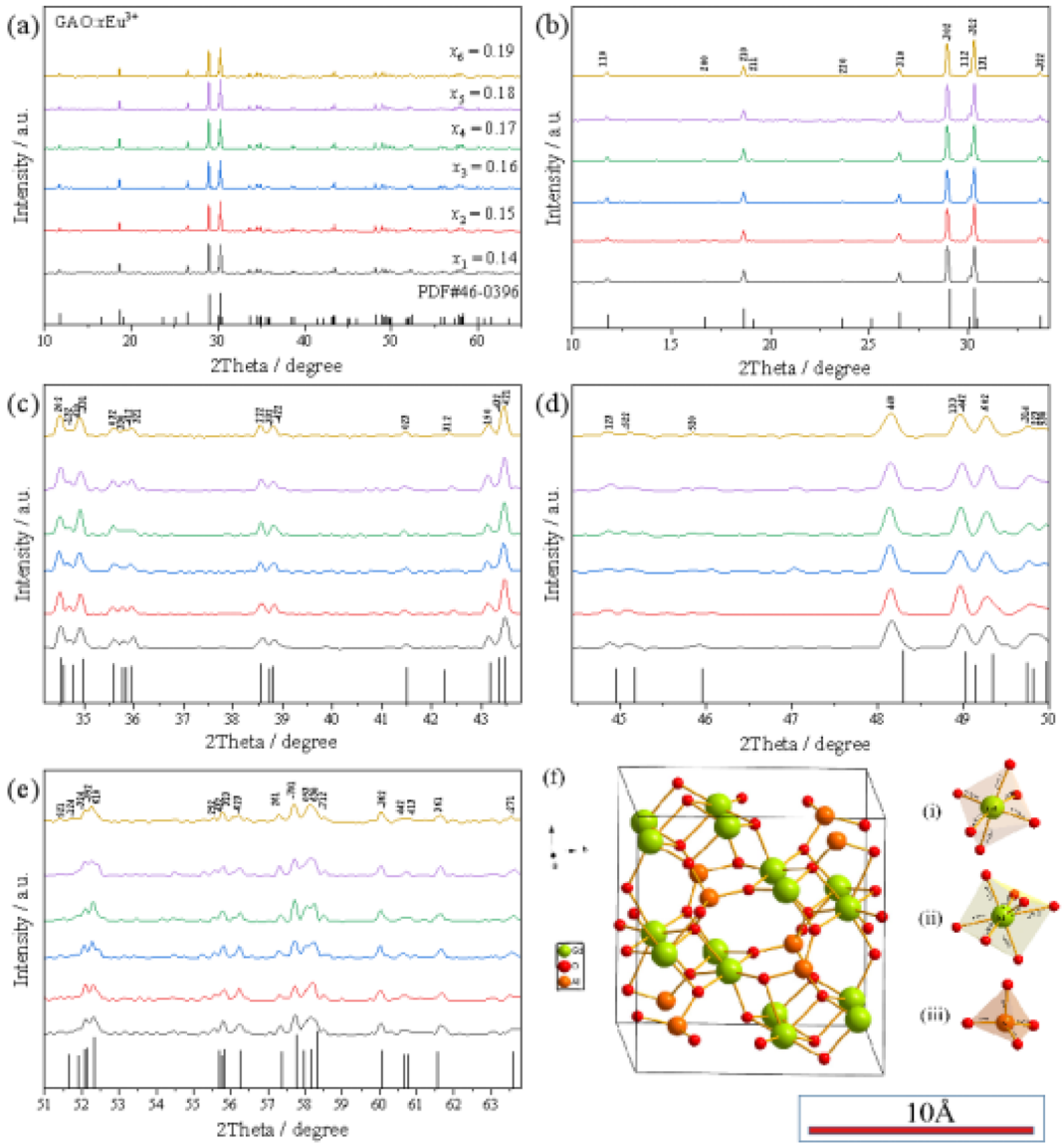

Fig. 1 The structure of samples: (a–e) XRD pattern of GAO:xEu^{3+}, (f) schematic diagram of three dimensional cell structure.

Table 1 XRD indexed results of GAO:0.16Eu^{3+}

Sample	a/Å	b/Å	c/Å	V/Å^3
GAO:0.16Eu^{3+}	11.255	10.669	7.580	859.31
PDF#46 – 0396	11.246	10.676	7.564	857.60

the difference in radius with Al^{3+} is large, so Eu^{3+} is more inclined than Al^{3+} to replace the Gd^{3+} lattice in GAO. Fig. 1(b) is the 3D cell structure schematic diagram of GAO, which shows the coordination between Gd^{3+} and O^{2-}, and Al^{3+} and O^{3+}, respectively. The crystal of GAO belongs to monoclinic structure[14] (PDF#46 – 0396). In GAO, Gd^{3+} is in two different positions: coordination with seven oxygen atoms to form GdO_7 polyhedra and coordination with six oxygen atoms to form GdO_6 octahedra, respectively. Al^{3+} coordination with four O^{2-} to form AlO_4 tetrahedral sites.[16]

Fig. 2 shows the SEM and EDS test results of the sample GAO:0.16Eu^{3+}. The SEM image shows that the sample is composed of irregular agglomerated particles with size of 1–5 μm. The EDS test results show the corresponding face scan of each element, showing that the sample consists of Gd, Al, O, Eu elements, and each element is uniformly distributed in the phosphor particles. This can prove that Eu^{3+} has been doped into the GAO.

3.2 Luminescence properties

Fig. 3(a) shows the PLE&PL spectra of the GAO:0.16Eu^{3+}. First, the PLE spectrum of GAO:0.16Eu^{3+} was obtained by monitoring the emission of $^5D_0 \rightarrow {}^7F_2$ at 610 nm. The strong broadband excitation peak in the 240–340 nm region is the charge transfer band of $O^{2-} \rightarrow Eu^{3+}$, resulting from the transition of electrons from the 2p orbital of O^{2-} to the 4f orbital of Eu^{3+} and the peak

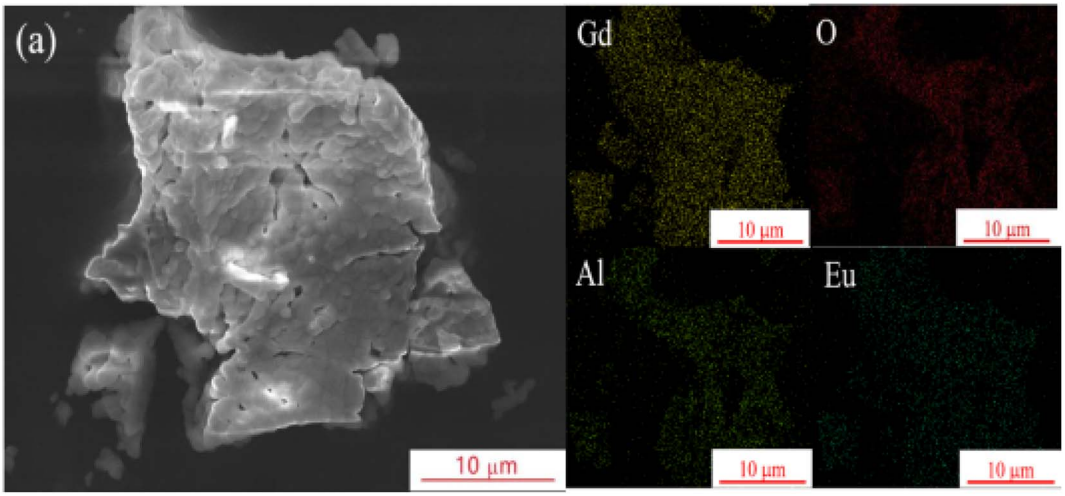

Fig. 2 SEM image and element mapping images of sample GAO:0.16Eu^{3+}.

is located at 274 nm. In addition, the charge transfer band of $O^{2-} \rightarrow Eu^{3+}$ overlaps with the peaks of Gd^{3+} at 274 nm ($^8S_{7/2} \rightarrow {}^6I_J$), 308 nm ($^8S_{7/2} \rightarrow {}^6P_{7/2}$) and 314 nm ($^8S_{7/2} \rightarrow {}^6P_{5/2}$), so that Eu^{3+} can receive energy from Gd^{3+} when the sample is excited at 274 nm, thus enhancing the emission. The presence of the $^8S_{7/2} \rightarrow {}^6I_J$ transition peak is direct evidence of the energy transfer of $Gd^{3+} \rightarrow Eu^{3+}$.[24] Fig. 3(b) shows the energy level transition of the energy transfer process of $Gd^{3+} \rightarrow Eu^{3+}$. When the GAO:0.16Eu^{3+} excited at 274 nm, the ground state electrons at the $^8S_{7/2}$ of Gd^{3+} are excited to the ^6I_J, with some electrons returning to the ground state by non-radiative transitions and others transferring to the $^5L_6$ energy level of Eu^{3+}. Because the ^6I_J energy level is higher than the $^5L_6$ energy level of Eu^{3+}, the energy transfer of $Gd^{3+} \rightarrow Eu^{3+}$ is irreversible. This

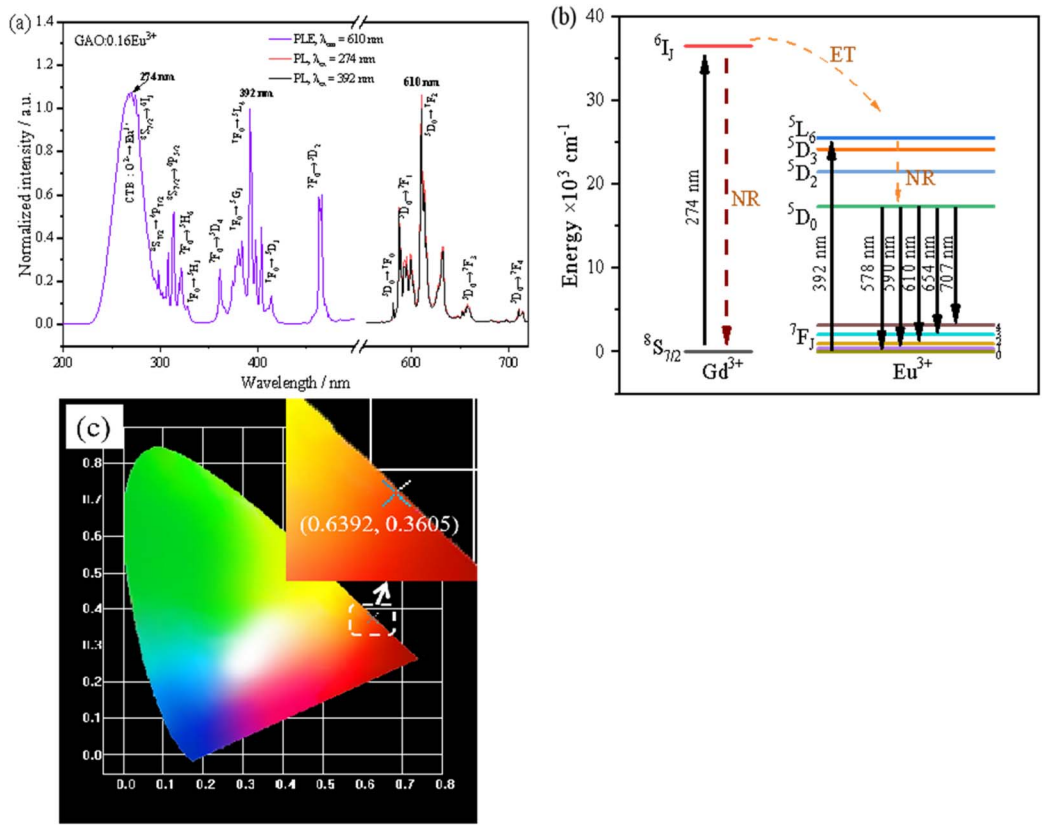

Fig. 3 The fluorescence characteristic of GAO:0.16Eu^{3+}: (a) PLE&PL spectra, (b) mechanism of energy transfer process of $Gd^{3+} \rightarrow Eu^{3+}$, (c) chromaticity diagram.

phenomenon was also observed in the GAO:Eu^{3+} phosphor synthesized by co-precipitation and urea-assisted combustion methods.[14,15] Different from these two reports, our sample showed strong characteristic absorption peaks of Eu^{3+} in the range of 350–500 nm, the peaks at $^7F_0 \rightarrow {}^5H_6$ (321 nm), $^7F_0 \rightarrow {}^5H_3$ (327 nm), $^7F_0 \rightarrow {}^5D_4$ (361 nm), $^7F_0 \rightarrow {}^5G_3$ (384 nm), $^7F_0 \rightarrow {}^5L_6$ (392 nm), $^7F_0 \rightarrow {}^5D_3$ (414 nm), $^7F_0 \rightarrow {}^5D_2$ (466 nm), are ascribed to 4f–4f transitions of Eu^{3+} ions. In the PLE part, the strongest absorption peak of the sample was located at 274 nm and the secondary absorption peak was located at 392 nm, moreover, the peak of the secondary absorption peak was 93.98% of the value of the strongest absorption peak, which indicated that our prepared GAO:0.16Eu^{3+} phosphor was able to work at two different excitation wavelengths of 274 nm and 392 nm, respectively.

The PL portion of Fig. 3(a) is described as follows: emission spectra obtained from GAO:0.16Eu^{3+} phosphors excited by 274 nm (red line) and 392 nm (blue line). The PL spectra excited by 392 nm and 274 nm differ only in intensity, the integrated luminescence intensity obtained for GAO:0.16Eu^{3+} under 392 nm excitation (integration range: 570–720 nm) is 92.65% of that obtained under 274 nm excitation. The weak emission peaks at 578, 590, 654 and 707 nm were due to the transitions of Eu^{3+} ion from $^5D_0$ to $^7F_0$, $^7F_1$, $^7F_3$ and $^7F_4$ levels, respectively. The strongest emission peak around 610 nm were assigned to the Eu^{3+} electric dipole transition of $^5D_0 \rightarrow {}^7F_2$, so that Eu^{3+} is in a non-inversion symmetry site in the GAO. Our aim is to explore high-temperature red phosphors with near-UV excitation, so follow-up analysis was performed with data obtained from samples excited under 392 nm.

Fig. 3(c) obtained from PL spectrum excited by 392 nm excitation in Fig. 3(a), which shows that the luminescence of the sample is in the red region, and the emission spectrum data were converted to color coordinates (0.6392, 0.3605) by the calculation software "1931CIE". To find out the color purity of the sample GAO:0.16Eu^{3+}, the color purity (CP) can be calculated by the following equation:[25]

$$CP = \frac{\sqrt{(x - x_i)^2 + (y - y_i)^2}}{\sqrt{(x_d - x_i)^2 + (y_d - y_i)^2}} \times 100\% \quad (1)$$

where (x, y) denotes the color coordinates of the different samples studied, (x_i, y_i) denotes the CIE value of an equal-energy light source with coordinates (0.3333, 0.3333), and (x_d, y_d) is the chromaticity coordinate corresponding to the main wavelength of the light source, which in this experiment is (x_d, y_d) = (0.1063, 0.0945). The color purity of GAO:0.16Eu^{3+} was calculated to be 95.7%.

3.3 Luminescent properties at different concentrations of Eu^{3+}

The emission intensity of GAO with different concentrations of Eu^{3+} was shown in Fig. 4(a). The PL intensity increased with

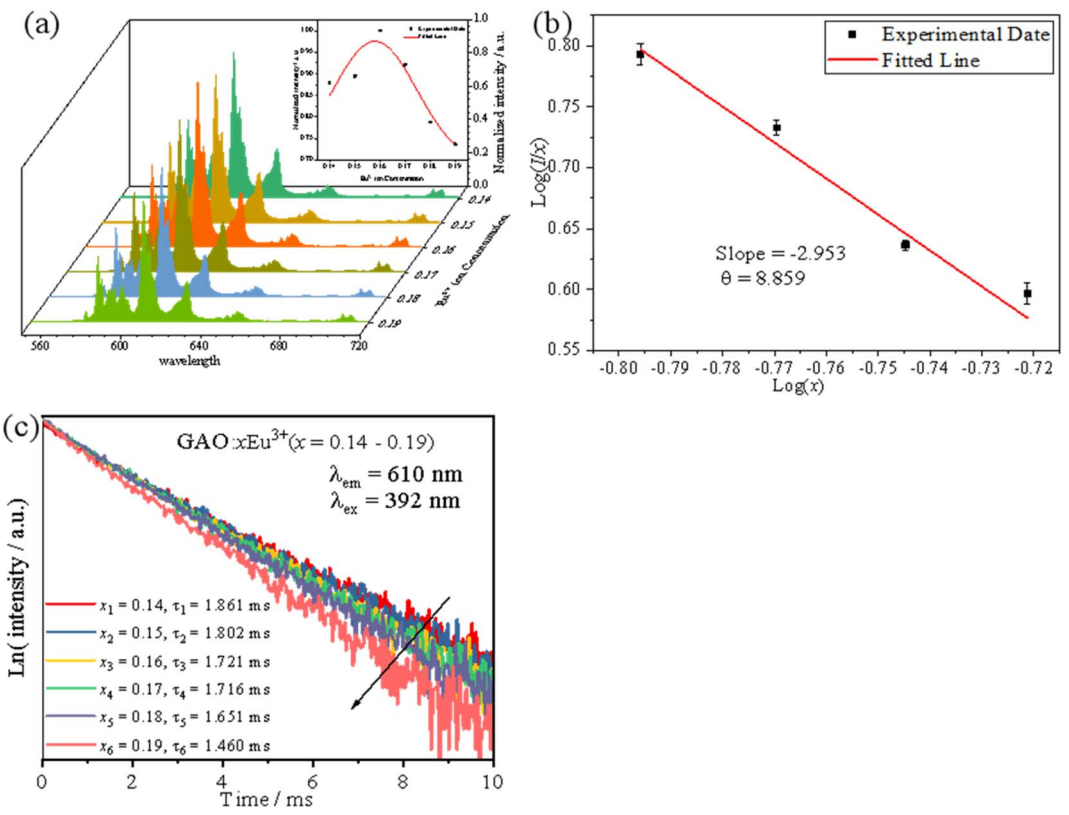

Fig. 4 Luminescent properties at different concentrations of Eu^{3+}: (a) PL spectra of GAO:x Eu^{3+} (x = 0.14, 0.15, 0.16, 0.17, 0.18 and 0.19), (b) the linear fitting curve of log(I/x) ~ log(x), (c) emission decay curves.

increasing Eu^{3+} ion concentration, reaching a maximum at 16 mol%, and then decreased with increasing Eu^{3+} ion concentration due to concentration quenching. With respect to the mechanism of energy transfer in phosphors, Blasse has pointed out that the critical transfer distance (R_c) at which the probability of transfer was equal to the probability of radiative emission, can be calculated using the formula:[26]

$$R_c \approx 2\left(\frac{3V}{4\pi x_c N}\right)^{\frac{1}{3}} \quad (2)$$

where V: volume of the unit cell, x_c: critical concentration of the activator ion and N: cations in the unit cell. By taking the experimental and analytical values of V, x_c and N as 0.8593 nm^3, 0.16 and 4 respectively. The critical transfer distance of Eu^{3+} in GAO:Eu^{3+} was calculated to be R_c = 1.367 nm. Since R_c = 1.367 nm was bigger than 0.5 nm, exchange interaction was not responsible for non-radiative energy transfer process from one Eu^{3+} ion to another Eu^{3+} ion in this host material.

In general, the concentration quenching effect works by activating three types of energy transfer between ions: mutual exchange interaction, radiation resorption and electrical multipole interaction. Reciprocal exchange can only be accomplished at R_c less than 0.5 nm. As for the radiation reabsorption mechanism, the excitation and emission spectra of the GAO:0.16Eu^{3+} phosphor do not have a clear overlap region. Therefore, in GAO:0.16Eu^{3+}, electric multipole interactions should dominate the concentration burst effect of Eu^{3+}. The type of electrical multilevel interaction can be judged by the following equation:[27,28]

$$\frac{I}{x} = K\left[1 + \beta(x)^{\theta/3}\right]^{-1} \quad (3)$$

where I and x represent the fluorescence intensity and activator concentration, respectively. K and β are the corresponding constants for the different interactions during the concentration quenching. The values of θ in this equation are 6, 8 and 10, corresponding to the electric dipole–electric dipole interaction, electric dipole–electric quadrupole interaction and electric quadrupole–electric quadrupole interaction, respectively. The relationship between $\log(I/x)$ and $\log(x)$ is plotted in Fig. 4(b), and a linear fit to the experimental data shows that θ = 8.859, which is closer to 8, implying that the concentration quenching of GAO:$x$$Eu^{3+}$ is caused by the energy transfer due to the electric dipole–electric quadrupole interaction.

Fig. 4(c) shows the fluorescence decline curves for GAO:$x$$Eu^{3+}$. The fit was performed with a single exponential equation as follows:[29]

$$I_t = I_0 + A\exp\left(\frac{-t}{\tau}\right) \quad (4)$$

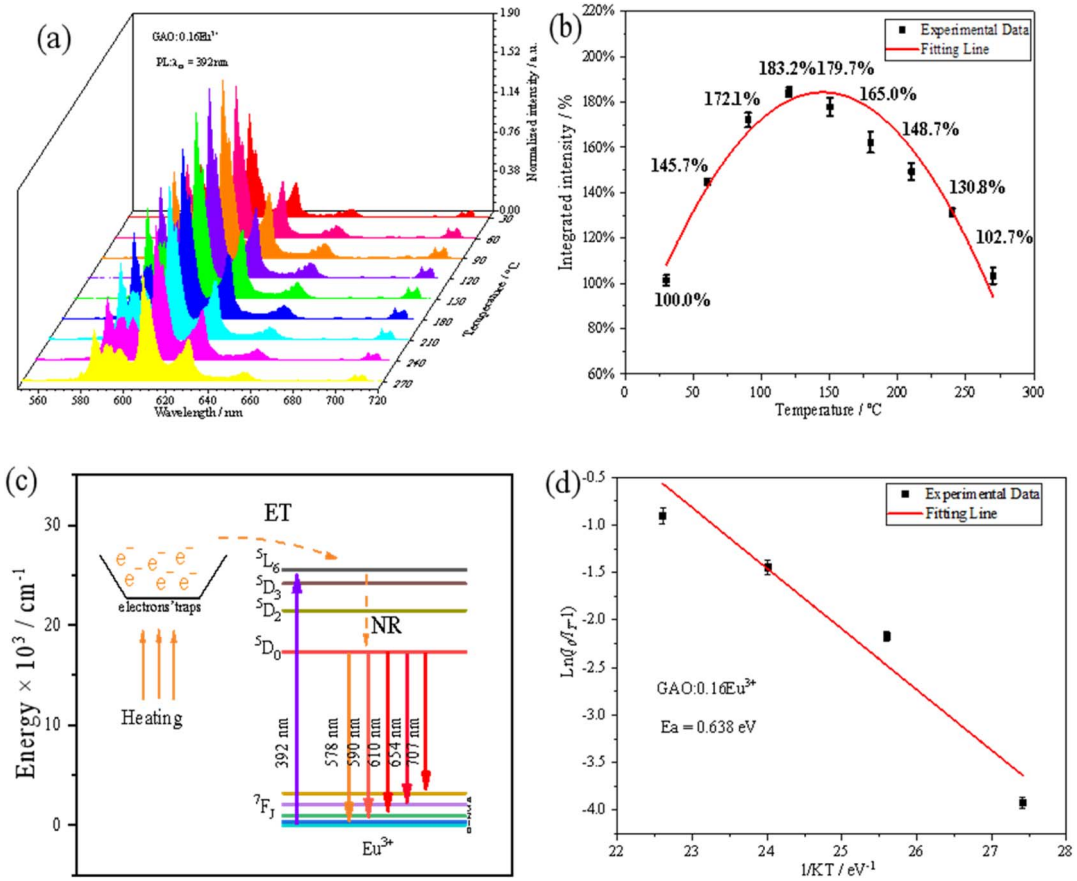

Fig. 5 Luminescent properties of GAO:0.16 Eu^{3+} at different temperatures: (a) PL spectra, (b) integrated intensity curves, (c) mechanism of negative thermal quenching, (d) activation energy curves of thermal quenching.

where I_t and I_0 represent the luminous intensity at time t and t_0 respectively, A is a constant and τ is the fluorescence lifetime. $x_1 = 0.14$, $x_2 = 0.15$, $x_3 = 0.16$, $x_4 = 0.17$, $x_5 = 0.18$ and $x_6 = 0.19$ correspond to fluorescence lifetimes of 1.861, 1.802, 1.721, 1716, 1.651, 1.460 ms, respectively. This means that the fluorescence lifetime tends to decrease as the doping concentration increases. This is due to the decrease in the average distance between Eu^{3+} due to the increase in doping concentration, which increases the chance of energy transfer and interaction between the ions, thus decreasing the fluorescence lifetime.

3.4 Luminescent thermal stabilities

The high-temperature fluorescence performance of the sample GAO:0.16Eu^{3+} was shown in Fig. 5(a) and (b). When the test temperature was increased from 30 °C to 120 °C, the emission of Eu^{3+} is enhanced with the increase of temperature, and the shape and position of the emission spectrum did not change. When the temperature reaches 120 °C, integrated intensity of the emission has a maximum value, and it is 183% of the initial one at 30 °C. When the temperature is over 120 °C, the luminous intensity decreases with the increase of temperature due to the thermal quenching effect, and at 270 °C, the integrated intensity is as high as 101.5% of the initial one at 30 °C, proving that GAO:0.16Eu^{3+} has an excellent luminous thermal stability.

The mechanism of NTQ effect has been discussed in a number of other reports.[30–32] That is, with the increasing of temperature, the electrons obtain energy compensation from the electron traps formed from the matrix defects and then they transfer the energy to Eu^{3+} to formation the effect,[33–36] which is described with Fig. 5(e). In this paper, electron traps formed from the substitution of Eu^{3+} for Gd^{3+} lattice sites that are in two different coordination sites.[33–36] The mechanism is shown in Fig. 5(c), where the number of excited electrons in Eu^{3+} through nonradiative relaxation to the ground state increases with increasing temperature, while electron traps are released from the defects into the $^5L_6$ energy level of Eu^{3+} upon heating, leading to an increase in the number of electrons in the radiative transition and thus enhanced emission of Eu^{3+}. In the whole high-temperature fluorescence test system, the only variable is the temperature of the phosphor. Due to the NTQ effect, the luminescence intensity of the sample is always stronger in the test temperature range (30–270 °C) than the initial one at 30 °C. First, the intensity is enhanced before 120 °C. The is attributed to radiative transition probability being larger than that of non-radiative transition, which is supported by energy compensation from the electron traps. Then, after 120 °C, the intensity weakened with the increase of temperature, due to high temperature quenching, which radiative transition probability is smaller than that of non-radiative

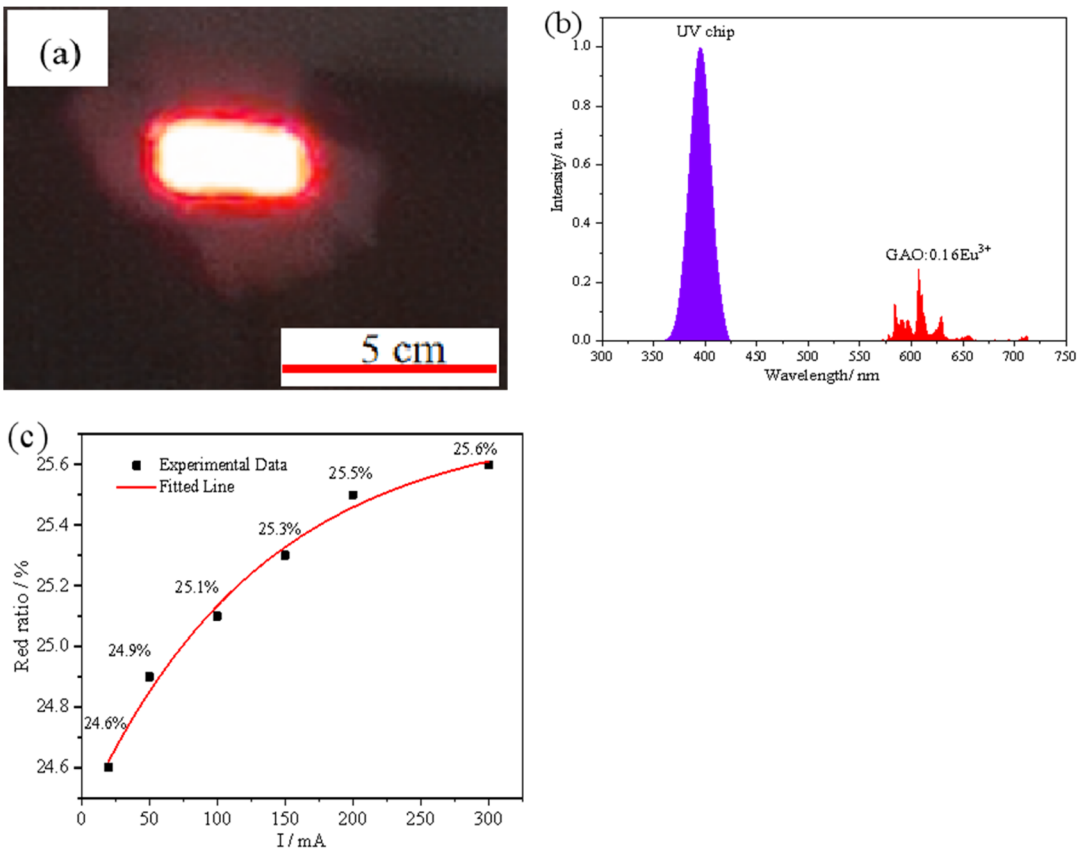

Fig. 6 Luminescent performances of prototype LEDs (GAO:0.16 Eu^{3+} +395 nm UV chip): (a) luminescence diagram under driving current of 20 mA, (b) electroluminescence spectra, (c) red ratio under a different drive current.

transition. From a macroscopic point of view, the mechanism of the NTQ effect should be considered as thermal-to-optical energy conversion mechanism.

In order to further understand the thermal stability of GAO:0.16Eu^{3+}, the thermal quenching activation energy of the samples was calculated by the Arrhenius equation based on the emission intensity of the samples at different temperatures, as shown in the following equation:[37]

$$I_T = I_0\left[1 + c\exp\left(-\frac{E_a}{KT}\right)\right]^{-1} \quad (5)$$

where I_T and I_0 represent the luminous intensities at temperature T and the initial intensity at room temperature, respectively; K represents the Boltzmann constant, c represents the substrate correlation constant and E_a represents the thermal burst activation energy of the material under study. The $\ln(I_0/I_T - 1) \sim 1/KT$ thermal quenching activation energy curve is shown in Fig. 5(d). The calculated activation energy $E_a = 0.638$ eV for the thermal quenching of GAO:0.16Eu^{3+}.

3.5 Luminescent performances of prototype red light LEDs

In order to further explore the performance of the sample GAO:0.16Eu^{3+} in actual working conditions, the sample GAO:0.16Eu^{3+} was assembled with a 395 nm UV chip to get a prototype red LED using a modified acrylate adhesive and tested under different driving currents, and the test results are shown in Fig. 6. Fig. 6(a) shows the luminescence of the assembled prototype red LED under a 20 mA drive current, and the sample emits bright red light under the excitation of 395 nm.

Fig. 6(b) shows the electroluminescence spectrum under 20 mA driving current, the purple emission band is the PL spectrum of the chip, and the red emission band is the PL spectrum of the sample, where red ratio of the LED is about 24.6%. Fig. 6(c) shows the variation of the red ratio of the prototype LED at different drive currents, which are 24.6%, 24.9%, 25.1%, 25.3%, 25.5%, and 25.6% at 20, 50, 100, 150, 200, and 300 mA drive currents, respectively. The temperature of the chip increases with the increase of the drive current, and the red-light ratio increases nonlinearly with the increase of the chip operating temperature in the range of 20 to 300 mA drive current, proving that there is a NTQ phenomenon in the actual use of the sample, which confirms the test results in Fig. 5(b).

4. Conclusions

In summary, we have synthesized a series of GAO:Eu^{3+} red emitting phosphors with high fluorescence thermal stability by combining the sol-gel method with high-temperature calcination. Their structure, morphology and composition, room temperature luminescence properties, NTQ effect and luminescence performance of the red LED prototypes were investigated in detail. The optimal sample GAO:0.16Eu^{3+} has strong absorption at both 274 nm and 392 nm and strong red emission at 610 nm with chromaticity coordinates of (0.6392, 0.3605). Surprisingly, GAO:0.16Eu^{3+} has a very excellent high-temperature fluorescence performance with the strongest integrated PL intensity at 120 °C, the corresponding integrated PL intensity is 183.2% of the initial value at 30 °C, and the luminescence intensity at the maximum test temperature of 270 °C still has 102.7% of the initial value at 30 °C. Therefore, GAO:0.16Eu^{3+} phosphor has a great potential to be used in the manufacture of the red part of WLEDs.

Author contributions

Junyu Ming: methodology, formal analysis, investigation, writing – original draft. Chaolian Luo: investigation. Shaokun Ling: investigation. Chang Chen: investigation. Yaxiong Wang: investigation. Sen Liao: conceptualization, supervision. Yingheng Huang: review & editing, visualization. Jie Liang: review & editing, visualization.

Conflicts of interest

The authors declare that they have no conflict of interest.

Acknowledgements

This research is supported by the National Natural Science Foundation of China (Grant No. 21661006 and No. 21965004), the Natural Science Foundation of Guangxi Zhuang Autonomous Region, China (Grant No. 2019GXNSFDA245022), the Scientific Research Foundation of Guangxi University (Grant No. XDZ140116), the innovation Project of Guangxi Graduate Education (Grant No. YCSW2020015), the Students Experimental Skills and Innovation Ability Training Fund Project of Guangxi University (No. S202210593143).

References

1 S. A. Khan, N. Z. Khan, M. Sohail, J. Ahmed, N. Alhokbany, S. M. Alshehri, X. Xu, J. F. Zhu and S. Agathopoulosf, *J. Mater. Chem. C*, 2021, **9**, 1341–1371.
2 Y. C. Lin, M. Karlsson1 and M. Bettinelli, *Top. Curr. Chem.*, 2016, **374**, 21.
3 E. Erol, N. Vahedigharehchopogh, O. Kıbrıslı, M. Ç. Ersundu and A. E. Ersundu, *J. Phys.: Condens. Matter*, 2021, **33**, 1–23.
4 L. Wu, Y. Bai, L. Wu, H. Yi, Y. Kong, Y. Zhang and J. Xu, *RSC Adv.*, 2017, **7**, 1146–1153.
5 X. Li, C. Yang, Q. S. Liu, X. C. Wang and X. Y. Mi, *Ceram. Int.*, 2020, **46**, 17376–17382.
6 J. Lakde, C. M. Mehare, K. K. Pandey, N. S. Dhoble and S. J. Dhoble, *J. Phys.: Conf. Ser.*, 2018, **18**, 8047–8069.
7 H. Guo, X. Y. Huang and Y. J. Zeng, *J. Alloys Compd.*, 2018, **741**, 300–306.
8 Z. Jia, X. L. Zhang, X. Y. Hua, Y. Dong, H. L. Li, C. Q. Feng, Y. G. Wang and M. J. Xia, *J. Alloys Compd.*, 2020, **844**, 155875.
9 K. Li and R. V. Deun, *Dyes Pigm.*, 2018, **155**, 258–264.
10 M. E. Alvarez-Ramosa, R. C. Carrillo-Torresa, R. Sánchez-Zeferinoa, U. Caldiñob and J. Alvarado-Rivera, *J. Non-Cryst. Solids*, 2019, **521**, 119462.

11 E. E. Hertle, L. Chepyga, A. Osvet, C. J. Brabec, M. Batentschuk, S. Will and L. Zigan, *Meas. Sci. Technol.*, 2019, **30**, 34001.
12 W. Chewpraditkul, N. Pattanaboonmee, O. Sakthong, W. Chewpraditkul, T. Szczesniak, M. Moszynski, K. Kamada, A. Yoshikawa and M. Nikl, *Opt. Mater.*, 2018, **76**, 162–168.
13 A. Morán-Ruiz, K. Vidal, A. Larrañaga and M. I. Arriortua, *Ceram. Int.*, 2018, **44**, 8761–8767.
14 D. Singh and S. Kadyan, *J. Mater. Sci.: Mater. Electron.*, 2017, **28**, 11142–11150.
15 J. Li, J. G. Li, L. Jing, S. Liu and Y. Sakka, *J. Solid State Chem.*, 2013, **206**, 104–112.
16 T. Deng and X. Jiang, *Opt. Mater.*, 2018, **78**, 27–34.
17 F. W. Kang, M. J. Peng, Q. Y. Zhang and J. R. Qiu, *Chem.–Eur. J.*, 2014, **20**, 11522–11530.
18 J. Y. Zhong, W. R. Zhao, F. Du, J. Wen, W. D. Zhuang, R. H. Liu, C. K. Duan, L. G. Wang and K. Lin, *J. Phys. Chem. C*, 2018, **122**, 7849–7858.
19 Y. Chen, Z. Y. Wang, W. G. Ding, X. Li, Q. Bao, J. J. Liu, K. L. Qiu, X. Y. Meng, Z. P. Yang and L. P. Li, *RSC Adv.*, 2019, **9**, 30406–30418.
20 J. Qiao, L. Ning, M. S. Molokeev, Y.-C. Chuang, Q. Liu and Z. Xia, *J. Am. Chem. Soc.*, 2018, **140**, 9730–9736.
21 S. Q. Fang, T. C. Lang, T. Han, J. Y. Wang, J. Y. Yang, S. X. Cao, L. L. Peng, B. T. Liu, A. N. Yakovlev and V. I. Korepanov, *Chem. Eng. J.*, 2020, **389**, 124297.
22 D. Zhao, Y. L. Xue and S. R. Zhang, *J. Mater. Chem. C*, 2019, **7**, 14264–14274.
23 S. H. Wang, Y. Q. Xu, T. Chen, W. H. Jiang, J. M. Liu, X. Zhang, W. Jiang and L. J. Wang, *Chem. Eng. J.*, 2021, **404**, 125912.
24 K. Upadhyay, R. K. Tamrakar and V. Dubey, *Superlattices Microstruct.*, 2015, **78**, 116–124.
25 Q. Dong, F. Yang, J. Cui, Y. Tian, S. Liu, F. Du, J. Peng and X. Ye, *Ceram. Int.*, 2019, **45**, 11868–11875.
26 L. Jing, X. Liu and Y. Li, *J. Lumin.*, 2015, **158**, 351–355.
27 A. Hooda, A. Khatkar, S. Chahar, S. Singh, P. Dhankhar, S. P. Khatkar and V. B. Taxak, *Ceram. Int.*, 2020, **46**, 4204–4214.
28 S. Chahar, R. Devi, M. Dalal, M. Bala, J. Dalal, P. Boora, V. B. Taxak, R. Lather and S. P. Khatkar, *Ceram. Int.*, 2019, **45**, 606–613.
29 S. Y. Xin, F. G. Zhou, L. Zhao, B. T. Liu, C. Wang, X. J. Wang, Z. W. Li and G. Zhu, *ECS J. Solid State Sci. Technol.*, 2018, **7**, R94–R98.
30 F. Kang, M. Peng, Q. Zhang and J. Qiu, *Chem.–Eur. J.*, 2014, **20**, 11522–11530.
31 J. Y. Zhong, W. R. Zhao, F. Du, J. Wen, W. D. Zhuang, R. H. Liu, C. K. Duan, L. G. Wang and K. Lin, *J. Phys. Chem. C*, 2018, **122**, 7849–7858.
32 W. Wang, M. Q. Fu, S. W. Liu, X. Y. Zhang, Y. Wei and G. G. Li, *J. Lumin.*, 2022, **242**, 118536.
33 S. Q. Fang, T. C. Lang, T. Han, J. Y. Wang, J. Y. Yang, S. X. Cao, L. L. Peng, B. T. Liu, A. N. Yakovlevb and V. I. Korepanovb, *Chem. Eng. J.*, 2020, **389**, 124297.
34 X. T. Fan, W. B. Chen, S. Y. Xin, Z. C. Liu and M. Zhou, *J. Mater. Chem. C*, 2018, **6**, 2978–2982.
35 J. Y. Ming, Y. X. Wang, S. K. Ling, S. Liao, Y. H. Huang and H. X. Zhang, *Inorg. Chem. Commun.*, 2021, **127**, 108549.
36 D. Zhao, Y. L. Xue and S. R. Zhang, *J. Mater. Chem. C*, 2019, **7**, 14264–14274.
37 L. Zhao, F. Y. Fan and X. Chen, *J. Mater. Sci.: Mater. Electron.*, 2018, **29**, 5975–5981.